CHAPTER 7

Silver-loaded starch functionalized Fe_3O_4 with AgI heterostructure photocatalyst for H_2O_2 production and its in situ Fenton reaction

7.1 INTRODUCTION

In continuation of the previous chapter (Chapter 6), this chapter developed the Ag-loaded starch functionalized with AgI heterostructure photocatalysts. AgI was introduced as a reduction component by loading it onto the Ag-loaded starch-functionalized Fe_3O_4 photocatalyst to further enhance its photocatalytic activity. Specifically, the 10 wt% Ag-loaded starch-functionalized Fe_3O_4 (10ASM), which exhibited the highest H_2O_2 production efficiency in the previous study, was selected for AgI loading.

AgI exhibits promising characteristics as a photocatalyst attributed to its light-sensitive properties. AgI is commonly employed in photocatalysis owing to its remarkable ability to absorb visible light. Additionally, AgI has a favorable band gap (2.6-2.8 eV) and band edge potential, with a CB potential more negative than the $O_2/•O_2^-$ redox potential (–0.33 V vs. NHE), making it suitable for driving oxygen reduction reactions [29]. However, the practical use of pristine AgI is restricted by its larger particle sizes and poor photostability [29,148]. In contrast, combinations of AgI with other semiconductors significantly enhance photostability and photocatalytic activity by promoting improved charge separation. For instance, the development of AgI composites such as AgI/UIO-66[235], Ag_2O/AgI [236], $CuWO_4$/AgI [148], Ag_3VO_4/AgI [237], AgI/g-C_3N_4 [238], AgI/Bi_2MoO_6 [239], AgI/$BiVO_4$ [240], AgI/BiOBr [241], AgI/$NiFe_2O_4$ [29], etc., has demonstrated excellent photocatalytic activity under visible light.

Furthermore, recent studies have highlighted the role of plasmonic nanoparticles (such as Ag and Au) strategically positioned at the interface between two semiconductor components to enhance visible light absorption, promote charge carrier separation, and accelerate interfacial charge transfer. For instance, Ma et al. [65] developed a $Fe_2(MoO_4)_3$/Ag/Ag_3PO_4 heterojunction photocatalyst for photocatalytic H_2O_2 production.

The incorporation of Ag nanoparticles at the interface enhances visible light absorption and facilitates faster charge transfer from $Fe_2(MoO_4)_3$ to Ag_3PO_4 via a Z-scheme pathway. Similarly, various other photocatalysts have been developed for diverse photocatalytic applications. These include Ag|AgBr/Ag/$FeTiO_3$ [242], CeO_2 QDs/Ag/Ag_2Se [243], g-C_3N_4/Au/C-TiO_2 [244], Bi_2WO_6/Ag_3PO_4–Ag [245], AgI/NH_2-MIL-68(In/Fe) [246].

Based on the above discussion, in our study, Ag-loaded starch functionalized Fe_3O_4 with AgI were selected as candidates to construct a Z-scheme heterojunction. The designed system was prepared through the step-wise precipitation method. The Fe_3O_4 nanoparticles were functionalized with soluble starch to enhance the water oxidation properties. The AgI was incorporated with Ag-loaded SM because of the well-matched band alignment and strong reduction property of AgI. The composition, structure, morphology, optical properties, and band structure were investigated, and their photocatalytic performance was evaluated for the H_2O_2 production, as well as the in-situ utilization of the generated H_2O_2 for both dark Fenton and photo-Fenton reactions. The yield of in-situ generated H_2O_2 was determined by an iodometry method. Moreover, the photocatalytic mechanism of this cascade reaction is examined and proposed based on a series of control experiments. The novelty of this article lies in the fact that no prior research has been conducted on the in situ utilization of produced H_2O_2 for dark Fenton reactions.

7.2 EXPERIMENTAL SECTION

7.2.1 Preparation of starch-functionalized Fe_3O_4 and silver-loaded starch-functionalized Fe_3O_4

In the previous chapter (Chapter 6), the detailed synthesis protocols of starch-functionalized Fe_3O_4 and silver-loaded starch-functionalized Fe_3O_4 were discussed. The nomenclature and abbreviations of the prepared samples are presented in Table 7.1.

7.2.2 Preparation of (10 wt.% Ag-loaded starch-functionalized Fe_3O_4)/AgI photocatalyst

The required amount of previously prepared 10ASM photocatalyst was dispersed in 30 ml of DDW using the water bath sonication for 20 minutes. Afterward, different amounts (5, 10, 20, and 30 wt%) of AgI nanoparticles were precipitated onto the 10ASM sample using the precipitation method. A measured quantity of $AgNO_3$ solution of a particular concentration was added to the suspension of re-dispersed 10ASM nanoparticles. The mixture was then agitated on an adsorption shaker for 10 hours. This step was essential to facilitate the adsorption of Ag^+ ions onto the 10ASM sample. An appropriate amount of KI solution was added gradually to the previously obtained suspension, given the desired AgI content in the composite samples. The formed precipitate was washed multiple times with DDW and ethanol. Then, the resulting product was dried in an oven at 60 °C for 20 hours. For comparative analysis, two additional samples were prepared: 1) SM with a 20 wt% AgI nanocomposite and 2) Fe_3O_4 with a 20 wt% AgI nanocomposite (without starch). The nomenclature and abbreviations for the prepared nanocomposites are detailed in Table 7.1. Scheme 7.1 shows the schematic pathway of 10ASM/AgI heterostructure formation.

Table 7.1. Nomenclatures and abbreviations utilized for the photocatalysts examined in the ongoing investigation.

Samples	Abbreviations
Starch functionalized Fe_3O_4 nanoparticles	SM
AgI nanoparticles	AgI
10 wt% Ag-loaded SM nanoparticles	10ASM
ASM with 5 wt% AgI composite	10ASM /A1
ASM with 10 wt% AgI composite	10ASM /A2
ASM with 20 wt% AgI composite	10ASM /A3
ASM with 30 wt% AgI composite	10ASM /A4

Pure Fe_3O_4 (without starch) and 20 wt% AgI composite	M/A3
s-Fe_3O_4/20 wt% AgI composite	SM/A3

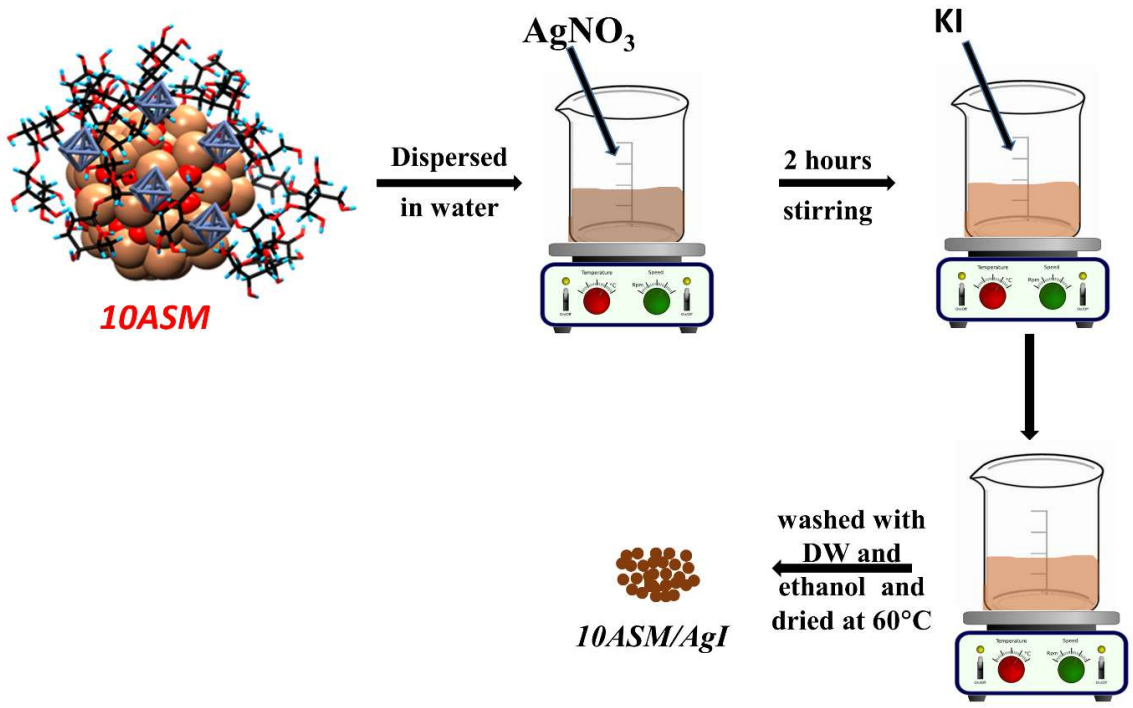

Scheme 7.1 Schematic representation of the preparation of 10ASM/AgI heterostructure photocatalysts

7.2.3 Photocatalytic test for H_2O_2 production

The photocatalytic activity of the synthesized SM, AgI, 10ASM/A1, 10ASM/A2, 10ASM/A3, 10ASM/A4, M/A3, and SM/A3 samples was evaluated for the H_2O_2 production under visible light irradiation. In each experiment, 3 mg of the as-prepared photocatalyst was dispersed in 20 mL of DDW within a quartz reactor. Before irradiation, the suspension was kept in the dark for 60 minutes. Afterward, the suspension was exposed to illumination using a cool white LED (1070 W/m^2) at ambient temperature. During the irradiation process, 2 ml of the suspension was extracted every 30 minutes, and the photocatalyst particles in it were magnetically separated. Next, H_2O_2 formation in the

reaction mixture (without photocatalyst particles) was analyzed spectroscopically by an iodometric method using a UV/VIS absorbance spectrophotometer. Additionally, photocatalytic experiments in pure water were conducted at different pH values (2, 3, 5, 7). Experiments were also carried out in different gas purging environments (O_2 and N_2) under optimum pH conditions. Besides pure water, photocatalytic experiments were also done in (5 vol%) aqueous solutions of various sacrificial reagents (ethanol, isopropanol, and glycerol). Active species trapping experiments were performed by introducing different scavengers during the photocatalytic H_2O_2 production process, including p-benzoquinone (PBQ) for $\cdot O_2^-$, $AgNO_3$ for the electron (e^-), and EDTA-2Na for the hole (h^+).

7.2.4 In-situ dark-Fenton degradation

In the preceding section, we examined the photocatalytic production of H_2O_2. Subsequent to the 120-minute duration of photocatalytic H_2O_2 production, 2.22 mL (~10ppm) of a tetracycline (TC) aqueous solution prepared from a 100 mgL^{-1} stock solution was introduced into the same reactor containing the photocatalytically produced H_2O_2 and underwent a dark Fenton reaction. At 15-minute intervals, 2.5 mL of TC aqueous solution was collected, and the photocatalyst was separated using an external magnet. The concentration of TC was measured using a UV/VIS absorbance spectrophotometer. Equation (7.1) was employed to calculate the degradation rate of TC.

$$D = \frac{C_0 - C_t}{C_0} \qquad (7.1)$$

Where 'D' represents the degradation rate, 'C_0' denotes the initial concentration of TC, and 'C_t' represents the final concentration of TC after a certain time of visible light illumination.

7.2.5 In-situ photo-Fenton degradation

Firstly, 3 mg of the photocatalyst was dispersed in 20 mL of a 10 mgL^{-1} TC aqueous solution. Subsequently, the reaction solution was placed in the dark for 30 min to reach the adsorption-desorption equilibrium of the organic pollutant. Next, the photocatalytic reaction was initiated when the above suspension was exposed to visible light. At 10-minute intervals, 2 mL of the TC solution was withdrawn, and the catalyst was separated magnetically by decantation. The concentration of TC was measured using a UV/VIS absorbance spectrophotometer. The degradation rate of TC was calculated from the above equation (7.1). Following the in situ Fenton reaction, the photocatalyst was collected and subsequently utilized again in the subsequent run under the same conditions.

7.3 RESULTS AND DISCUSSION

The crystal structures and phase-structural composition of the AgI, SM, 10ASM, M/A3, SM/A3, 10ASM/A1, 10ASM/A2, 10ASM/A3, and 10ASM/A4 catalysts were evaluated by performing XRD measurements. In Figure 7.1a, the XRD pattern displays the diffraction peaks of pristine SM at 2θ values of 18.31°, 30.20°, 35.53°, 37.28°, 43.21°, 47.39°, 53.87°, 57.30°, and 62.71° matched the (111), (220), (311), (222), (400), (331), (422), (511), and (440) crystal planes of the cubic phase of Fe_3O_4 (JCPDS File No. 88-0315). The XRD profiles of 10ASM (Ag nanostructures loading) reveal two additional distinct peaks at 2θ values of 38.16 and 44.31°, corresponding to the (111) and (200) crystal planes of the Ag phase (JCPDS File No. 87-0720). Similarly, the diffraction peaks of pristine AgI at 23.70°, 39.12°, 46.32°, and 62.25° can be assigned to the (111), (220), (311), and (331) cubic AgI (JCPDS File No. 78-0641)[148], respectively. The X-ray diffraction patterns of the four powder samples, namely 10ASM/A1, 10ASM/A2, 10ASM/A3, and 10ASM/A4, exhibit peaks indicative of Fe_3O_4, Ag, and AgI phases. This observation signifies the successful formation of the 10ASM/AgI nanocomposite photocatalyst, as

depicted in Figure 7.1a. Notably, the XRD patterns of 10ASM/AgI nanocomposites do not show any additional peaks, confirming the purity of the photocatalysts. On the other hand, Figure 7.1b shows the XRD pattern of M/A3 (Fe_3O_4/AgI nanocomposite) and SM/A3 (starch functionalized Fe_3O_4/AgI nanocomposites).

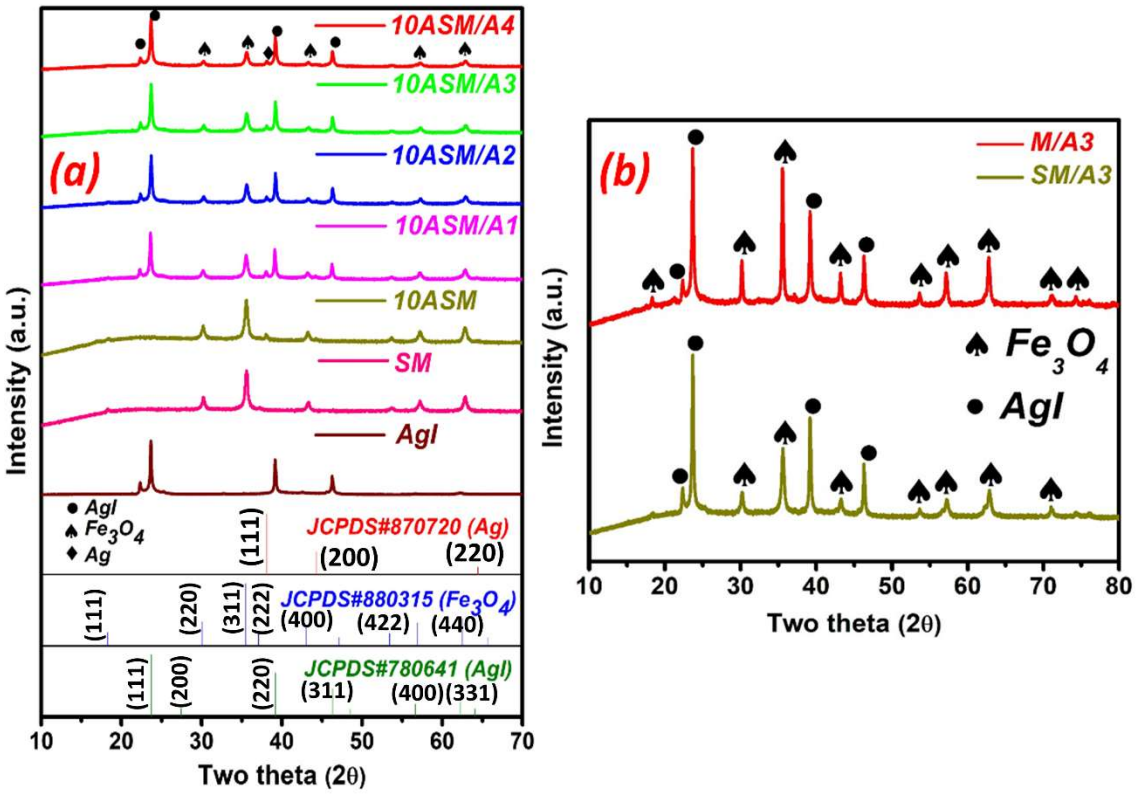

Figure 7.1. XRD patterns of **(a)** AgI, SM, 10ASM, 10ASM/A1, 10ASM/A2, 10ASM/A3, and 10ASM/A4 samples **(b)** SM/A3 and M/A3.

The morphologies of the SM, 10ASM, and 10ASM/A3 photocatalysts were examined using TEM and SEM techniques. In Fig. 7.2a, the TEM image illustrates the fine, nearly spherical shape of SM nanoparticles, with average sizes ranging from 8 to 11 nm. The inset images in Fig. 7.2a depict the HR-TEM image and inverse fast Fourier transform (IFFT) analysis of SM nanoparticles, revealing their interplanar spacing. The calculated interplanar spacing of 0.48 nm is attributed to the Fe_3O_4 (111) plane. In Fig. 7.2 (b and c), TEM and HR-TEM images of the 10ASM photocatalyst are presented. Two types of

interplanar spacing are observed in Fig. 7.2c, measuring d equals to 0.48 nm and 0.23 nm, corresponding to the Fe_3O_4 (111) and Ag (111) planes, respectively. This gives confirmation that Ag nanostructures loading on SM (10ASM) was successfully prepared.

In Fig. 7.2d, the TEM image of the 10ASM/A3 showed the 10ASM nanoparticles forming interfaces with the irregular-shaped particles of AgI. The HR-TEM image was captured at the interface of 10ASM/A3, revealing an interplanar distance of 0.37 nm, corresponding to the d-spacing of the (111) plane of the AgI (Figure 7.2e). Figure 7.2f displays the SEM image of 10ASM/A3 composite, indicating the fine 10ASM spherical nanoparticles over the AgI particles. Furthermore, Figure 7.2g illustrates the elemental mapping of the 10ASM/A3 photocatalyst, which reveals the presence and respective distribution of Ag, I, Fe, and O elements in the required stoichiometry. All the aforementioned results validate the successful preparation of the 10ASM/A3 composite.

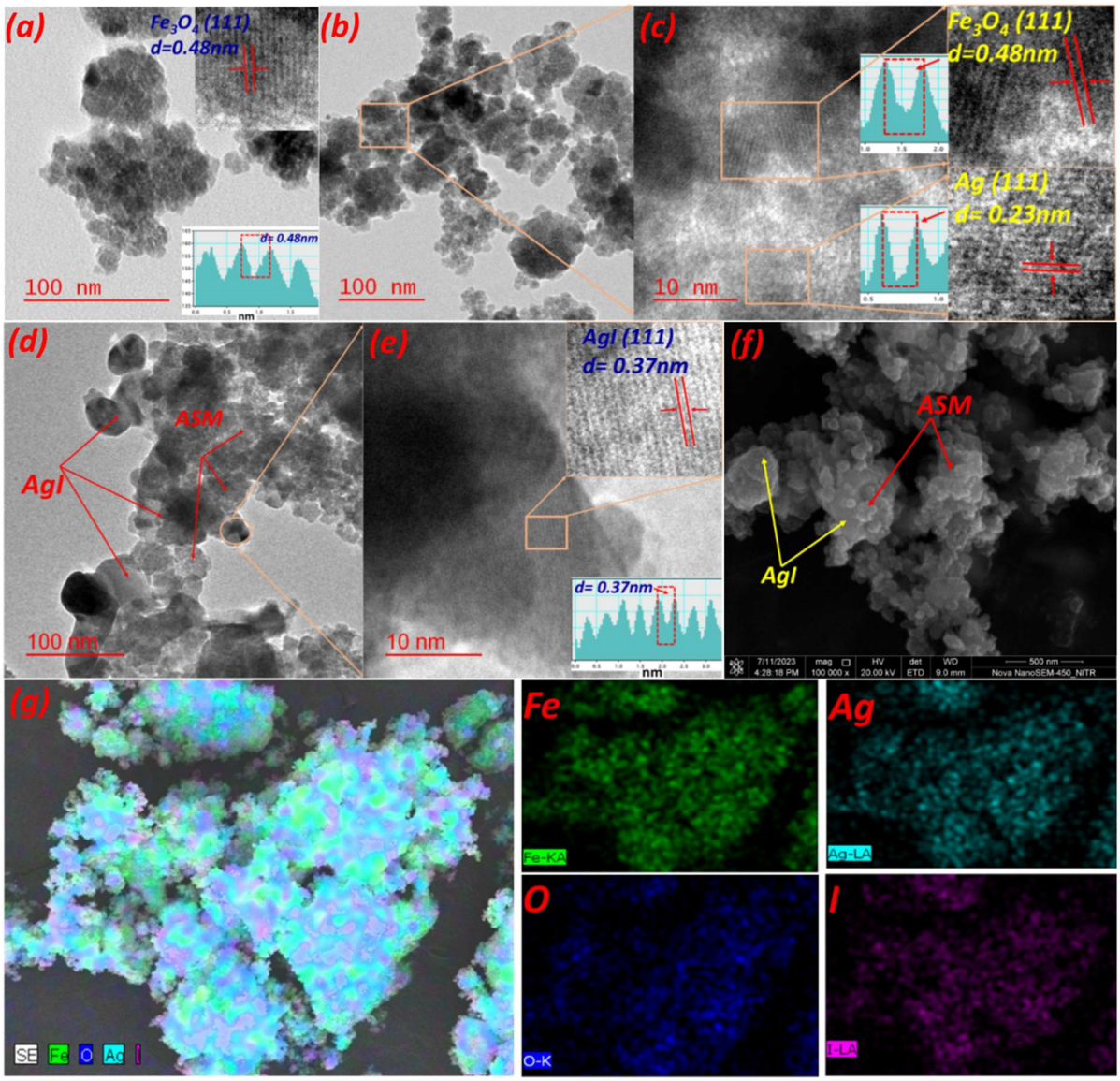

Figure 7.2. TEM images of **(a)** pure SM**, (b)** 10ASM sample**, (c)** HR-TEM images of 10ASM sample, and their inset IFFT analysis. **(d, e)** TEM and HR-TEM image of 10ASM/A3 sample**. (f)** SEM image of 10ASM/A3. **(g)** Elemental mapping of the 10ASM/A3 sample.

To determine the oxidation states, elements presents and electronic interaction, XPS was performed on four samples (AgI, SM, 10ASM, and 10ASM/A3). Fig. 7.3a the high resolution (HR) Fe 2p spectrum of the SM sample is positioned at 709.1 and 722.6 eV, which correspond to Fe $2p_{3/2}$ and Fe $2p_{1/2}$, respectively. The Fe 2p region was deconvulated into four peaks at binding energy 709.4eV, 711.5 eV, 722.4 eV, and 724.8eV corresponding

to $2p_{3/2}$ and $2p_{1/2}$ of Fe^{2+} and Fe^{3+} oxidation states. Additionally, the remaining two peaks situated at 717.4 eV and 731.9 eV were indicative of shake satellite peaks, affirming the purity and successful formation of the Fe_3O_4 phase (Fig. 7.3a). The O 1s spectral band of pure SM split into three peaks at binding energies of 529.4 eV, 531 eV, and 532.1 eV of SM (Fig. 7.3b). These peaks were assigned to the oxygen anion (O^{2-}) in Fe_3O_4 crystal lattice (M-O), hydroxide ions (OH^-) on the metal oxide surface (Os), and, physically/chemically adsorbed H_2O (Oc) (Fig. 7.3b) [247,248]. Upon loading Ag onto SM, the BE shifts slightly towards the positive side (higher BE) in the 10ASM sample in both the Fe 2p and O 1s XPS spectrum (Fig. 7.3 (a, b)). Similarly, upon incorporating AgI into the 10ASM sample (10ASM/A3 configurations), a positive shift in the BE was observed in both the Fe 2p and O 1s XPS spectra compared to the 10ASM sample, as can be seen in Fig. 7.3 (a, b).

The HR Ag 3d spectrum (Fig. 7.3c) shows two peaks at 368 and 374 eV. These are attributed to Ag $3d_{5/2}$ and Ag $3d_{3/2}$, deriving from the Ag^+ ion of AgI. These peaks exhibit a slight negative shift (lower BE) at 367.8 and 373.8 eV in the XPS spectrum of the 10ASM/A3 sample. Similarly, two distinct peaks corresponding to the I $3d_{5/2}$ and I $3d_{3/2}$ are observed in the high-resolution I 3d spectrum of pure AgI, located at 618.9 eV and 630.4 eV, respectively, as shown in Fig. 7.3d [29,148]. These peaks are attributed to the presence of I^- in AgI. After the formation of composite photocatalyst (10ASM/A3), the negative shift was observed in BE of I 3d. The shift in BE signifies the strong electronic interaction occurring between SM, Ag, and AgI nanoparticles within the composite system of 10ASM/A3. This shift also gives confirmation of charge transfer, occurring from the 10ASM to the AgI component.

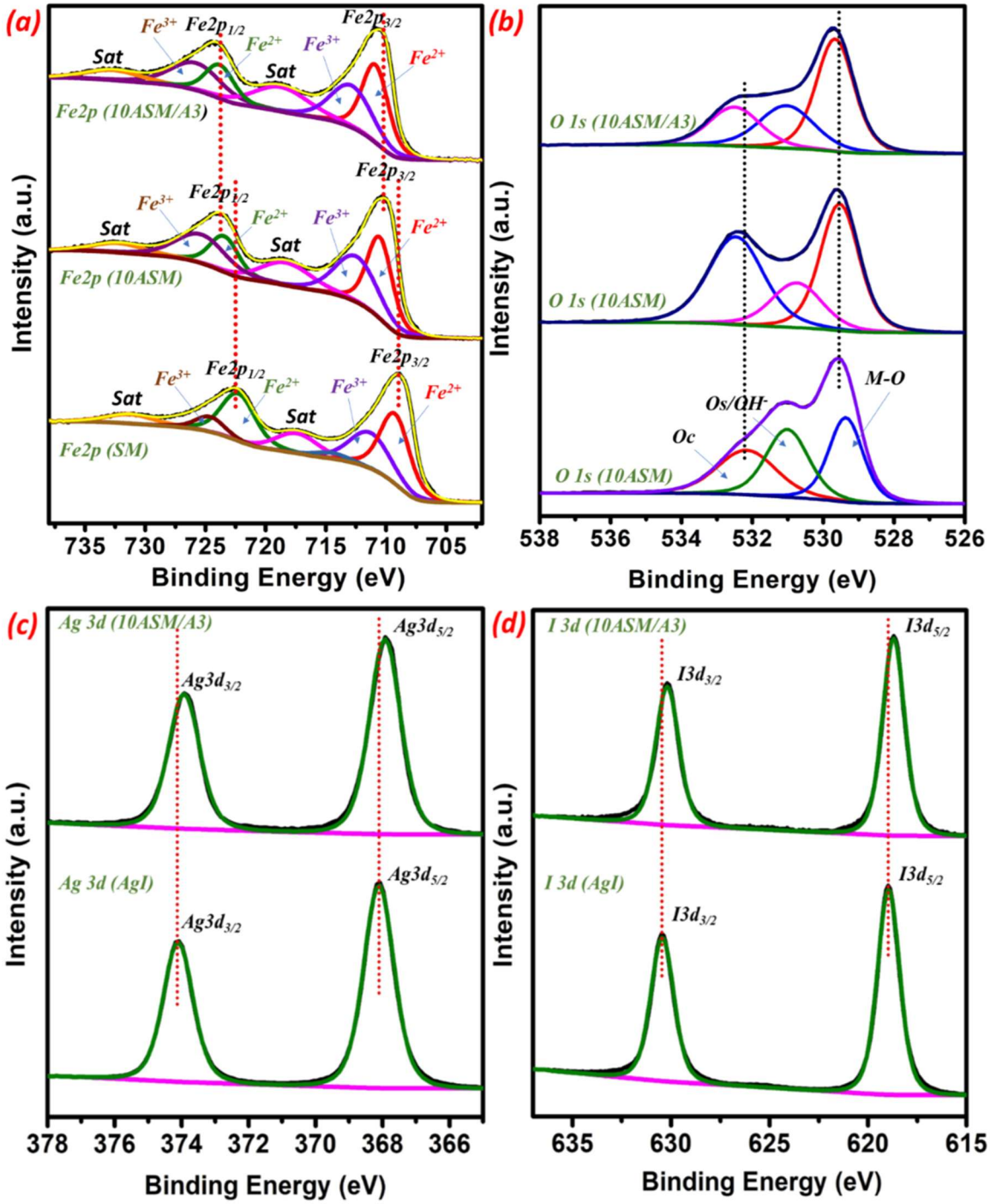

Figure 7.3. **(a, b)** XPS spectra of Fe 2p and O 1s of SM, 10ASM, and 10ASM/A3 sample; **(c, d)** XPS spectra of Ag 3d and I 3d of AgI and 10ASM/A3 sample.

Figure 7.4a illustrates the optical characteristics of SM, AgI, 10ASM, 10ASM/A1, 10ASM/A2, 10ASM/A3, and 10ASM/A4, as determined through UVDRS. The pure AgI exhibits an absorption edge at approximately 447 nm, while the pure SM shows an

absorption onset of around 560 nm. Notably, the 10ASM/AgI nanocomposite photocatalysts exhibit a red shift compared to pristine AgI, indicating enhanced visible light absorption. The graph in Figure 7.4b depicts $(\alpha h\nu)^2$ vs. hν, representing the band gap energy for pure AgI and SM. Through calculations, the band gap energies for SM and AgI are determined to be approximately 2.28 eV and 2.7 eV, respectively.

The potentials of the band edges and semiconductor types of SM and AgI nanoparticles were assessed using Mott-Schottky (MS) plots, as illustrated in Fig. 7.4 (c, d). The positive inclinations in the graph of $1/C^2$ observed for SM and AgI indicate that both exhibit n-type semiconductor behavior. The positioning of the conduction bands in SM and AgI nanoparticles was determined to be 0.28 V and -0.59 V, respectively. This observation validates the formation of a n-n (Z-scheme) heterojunction. Correspondingly, the valence band positions were calculated by integrating the MS data with the band gap values of SM and AgI employing the equation $E_{VB} = E_{CB} + E_g$. Given their energy gap of 2.28 eV (SM) and 2.7 eV (AgI), the valence band positions for SM and AgI were calculated to be 2.56 V and 2.11 V, respectively (Fig. 7.4 (c, d)).

For all measurements, the potential versus the Ag/AgCl reference electrode is transformed into the potential versus the Normal Hydrogen Electrode (NHE) using the equation V(NHE) = V(Ag/AgCl) + 0.059 pH + 0.197.

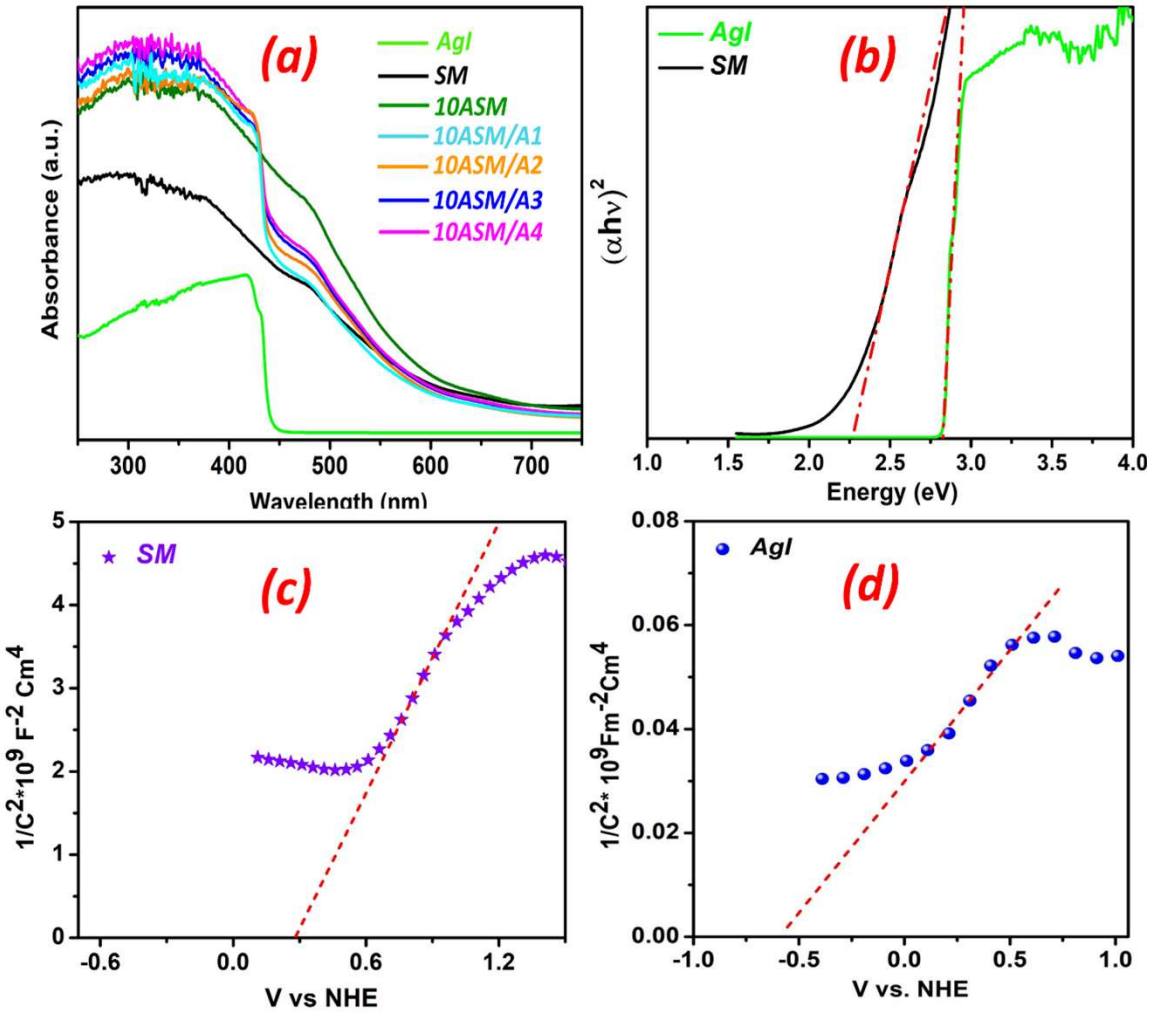

Figure 7.4. (a) UV-DRS absorbance spectra of the as-prepared sample (labeled in Fig. a). **(b)** Tauc plot of SM and AgI samples. Mott-schottky plot of **(c)** SM and **(d)** AgI.

The investigation of photo-excited charge separation and recombination efficiency was conducted through photoluminescence (PL) analysis. The PL spectrum indicates that, at the excitation wavelength of 340 nm (Figure 7.5a), the intensity of 10ASM/A3 is notably the lowest. This reduction in PL peak intensity serves as a clear indicator of improved interfacial charge separation and decreased rates of electron-hole recombination. Furthermore, the Electrochemical Impedance Spectroscopy (EIS) illustrates that 10ASM/A3 displays the smallest semicircle radius, providing confirmation of its faster interface charge transfer rate (Fig. 7.5b). A smaller value of charge transfer resistance (Rct)

signifies a higher efficiency in charge transfer within the system. The order of Rct values is as follows: SM (29.8 Ω) > 10ASM (11.7 Ω) > 10ASM/A1 (9.8 Ω) >10ASM/A2 (9.5 Ω) > 10ASM/A4 (7.3 Ω) >10ASM/A3 (5.7 Ω), aligning with the increased activity sequence of the photocatalysts. Notably, the Rct of the 10ASM/A3 (5.7Ω) is the smallest among all the photocatalysts. Consequently, this suggests that photo-generated electron-hole pairs are most effectively separated on the 10ASM/A3 catalyst, thereby enhancing the photocatalytic activity.

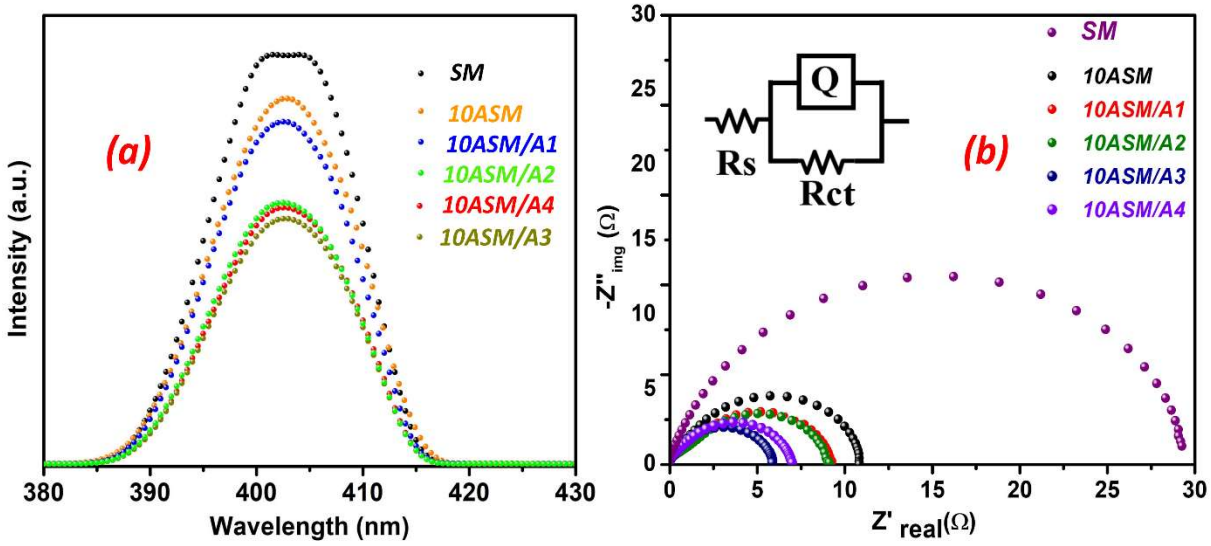

Figure 7.5. (a) PL emission spectra and **(b)** EIS analysis of photocatalysts (labeled in both Fig. 7.5a and 7.5b).

VSM was employed to investigate the magnetic properties of the best photocatalyst (10ASM/A3) samples, as displayed in Figure 7.6. The saturation magnetization of the 10ASM/A3 samples was determined at 15.78 emu/g. The magnetic hysteresis loops exhibit an absence of hysteresis, remanence, and coercivity, indicating the superparamagnetic nature of the resultant samples. Meanwhile, the 10ASM/A3 saturation magnetization is sufficient enough to recover the photocatalyst from a solution using an external magnetic field, as depicted in Figure 7.6 (inset picture).

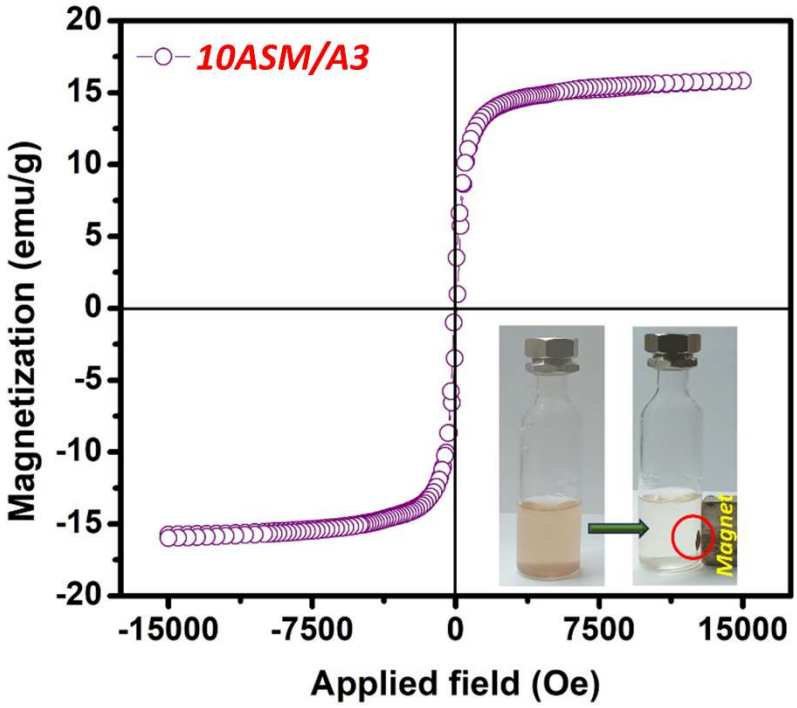

Figure 7.6. Magnetization curve of the 10ASM/A3 sample.

7.3.1 Photocatalytic result for H_2O_2 production

The photocatalytic H_2O_2 production capability of the prepared photocatalysts was evaluated in various conditions under visible-light irradiation. The initial test for photocatalytic H_2O_2 production was conducted without the presence of a catalyst, resulting in no observed H_2O_2 production. Additionally, the H_2O_2 production using different photocatalysts was investigated in the absence of light, and no H_2O_2 was detected, as shown in Figure 7.7. The H_2O_2 production rates over pristine SM, AgI, and metallic Ag-loaded SM (10ASM) after 60 minutes of visible light irradiation are 7 $\mu molg^{-1}h^{-1}$, 18 $\mu molg^{-1}h^{-1}$ and 165 $\mu molg^{-1}h^{-1}$ respectively, in neutral pH water without any sacrificial agents and O_2 bubbling, showcasing their potential for photocatalytic H_2O_2 production (Figure 7.7 and Figure 7.8a). The 10ASM photocatalyst, notably, demonstrated superior performance compared to pure SM and AgI, leading to efficient charge separation and minimizing

recombination. Consequently, it was selected for AgI loading to further improve the photocatalytic H_2O_2 production activity. Fig. 7.8a shows the time course of photocatalytic H_2O_2 production on pure AgI, 10ASM/A1, 10ASM/A2, 10ASM/A3, and 10ASM/A4. In comparison, all AgI-containing 10ASM photocatalysts demonstrate significantly improved efficiency in the production of photocatalytic H_2O_2. Specifically, 20 wt% AgI loading 10ASM photocatalyst (10ASM/A3) exhibits the highest performance in photocatalytic H_2O_2 production, with a generated H_2O_2 concentration reaching 712 $\mu molg^{-1}h^{-1}$ in pure water. This is more than 39 times that of pure AgI and approximately 4.3 times higher than the 10ASM photocatalyst. However, when the AgI loading on 10ASM surpasses 20 wt.% %, the composite photocatalyst (10ASM/A4) experiences a gradual decline in activity for photocatalytic H_2O_2 production (Figure 7.8a). This occurrence is likely attributed to the excessive AgI loading on the 10ASM, leading to light scattering and impeding the characteristics of 10ASM in the 10ASM/A4 composite photocatalysts. Hence, a loading of 20 wt % AgI is considered optimal for further experiments, and the remaining control experiments are conducted on the 10ASM/A3 composite sample. Usually, the production of H_2O_2 is favored under acidic conditions. Therefore, the effects of solution pH on the photocatalytic efficiency of H_2O_2 generation were also investigated using only the best photocatalyst (10ASM/A3). Nevertheless, the 10ASM/A3 composite exhibits the capability to sustain H_2O_2 production rates across a broad pH range, from 2 to 7. The results showed that 10ASM/A3 exhibited the best H_2O_2 production activity at pH 3, approximately 1615 μmol/g of H_2O_2 in 120 minutes (refer to Fig. 7.8b). The more acidic pH solution, such as pH 2, provides excess protons (H^+) to the reaction medium, thereby facilitating the formation of H_2O_2, which can then oxidize to water ($H_2O_2 + 2H^+ + 2e^- = 2H_2O$). Conversely, higher pH solutions, such as pH 5 and 7, reduce proton availability, leading to decreased

H_2O_2 formation. Therefore, pH 3 was determined to be the optimal pH value for H_2O_2 production [227].

The experiments for producing photocatalytic H_2O_2 were also carried out using 10ASM/A3 under different atmospheric gases (Air, O_2, and N_2). As illustrated in Fig. 7.8c, the H_2O_2 production rate under O_2-bubbling conditions showed a predominant enhancement, approximately 1.65 times higher than in normal atmospheric conditions (pure water at pH 3). In contrast, when O_2 was replaced with N_2, the amount of H_2O_2 produced on the 10ASM/A3 was reduced by 3.16 times compared to that under O_2-saturated conditions. This observation suggests that O_2 plays a crucial role in the photocatalytic H_2O_2 production. However, a significant amount of H_2O_2 continues to form (465 $\mu molg^{-1}h^{-1}$) even in the presence of an N_2-saturated environment. This control experiment suggests that O_2 is produced through the water oxidation pathway on the surface of the 10ASM/A3 photocatalyst, followed by the formation of H_2O_2 through the O_2 reduction reaction.

In Fig. 7.8d, the photocatalytic H_2O_2 production with various sacrificial agents, namely ethanol, isopropanol (IPA), and glycerol, serving as electron donors. As illustrated, the amount of generated H_2O_2 obtained with ethanol, IPA, and glycerol is 1956 μmol/g/h, 2102 μmol/g/h, and 2367 μmol/g/h, respectively. The photocatalytic H_2O_2 yield in the presence of glycerol was ~1.6 times higher than that of the absence of a sacrificial agent at pH 3 under O_2 bubbling. The comparison (Figure 7.8g) clearly demonstrates that the 10ASM/A3 photocatalyst used in this study outperforms the majority of known and recently published composite-based photocatalysts. Detailed experimental information regarding the photocatalytic H_2O_2 production of the compared catalytic systems is provided in Table 7.2. To further investigate the stability and recyclability of 10ASM/A3, we collected the photocatalyst through magnetic decantation and employed it in the next

experimental cycles. Even after five cycles, the quantity of H_2O_2 generated remained notably high, confirming the long-term stability and reproducibility of the 10ASM/A3 composite photocatalyst. The H_2O_2 yield exhibited only a marginal decrease (~4 %) in the last run (shown in Fig. 7.8e). Additionally, Figure 7.9h shows the XRD patterns of 10ASM/A3 before and after five cycles of the photocatalytic reaction. The results indicate that the crystal structure of 10ASM/A3 remains largely unchanged after the stability test, closely resembling that of the fresh sample. However, a slight shift towards lower 2θ values was observed in the XRD pattern, which may be attributed to surface corrosion or oxygen passivation of the catalyst caused by continuous oxygen bubbling during photocatalytic H_2O_2 production.

Scavenger experiments were conducted to investigate the H_2O_2 production mechanism or involvement of active species during the photocatalysis reaction on 10ASM/A3. Upon introducing $AgNO_3$ as an electron-trapping agent, there was a significant reduction in H_2O_2 yield, suggesting that H_2O_2 resulted from the photogenerated electron reduction of O_2 (Fig. 7.8f). Furthermore, the addition of p-BQ as $\bullet O_2^-$ trapping agents distinctly inhibited H_2O_2 production. This indicated that the photogenerated electron reduction of O_2 led to the generation of the $\bullet O_2^-$ intermediate product, which then combined with two protons (H^+) and underwent a photogenerated electron reduction to produce H_2O_2. This process corresponds to the two-step oxygen reduction reaction ($O_2 + e^- \rightarrow \bullet O_2^-$; $\bullet O_2^- + 2H^+ + e^- \rightarrow H_2O_2$). Nitroblue tetrazolium (NBT) experiments (Figure 7.9) further confirmed the presence of $\bullet O_2^-$. The absorbance of the NBT peak at ~265nm is diminished significantly with the reaction time in the presence of ASM/A3 photocatalyst under visible light irradiation, indicating the rapid formation of $\bullet O_2^-$ species [49]. These collective findings strongly support the formation of the $\bullet O_2^-$ intermediate species. Ethylenediaminetetraacetic acid disodium salt (EDTA-2Na) was also utilized to scavenge

the photogenerated holes (h^+), as shown in Figure 7.8f. The addition of EDTA-2Na in a photocatalytic system sluggish the H_2O_2 production rate by ~50% compared to normal atmospheric conditions, suggesting that h^+ is also the primary active species during the photocatalytic reaction. Consequently, it can be inferred that e^-, $\bullet O_2^-$, and h^+ species play a crucial role in the H_2O_2 production through two successive one-electron processes and water oxidation (Equations (7.2 and 7.3).

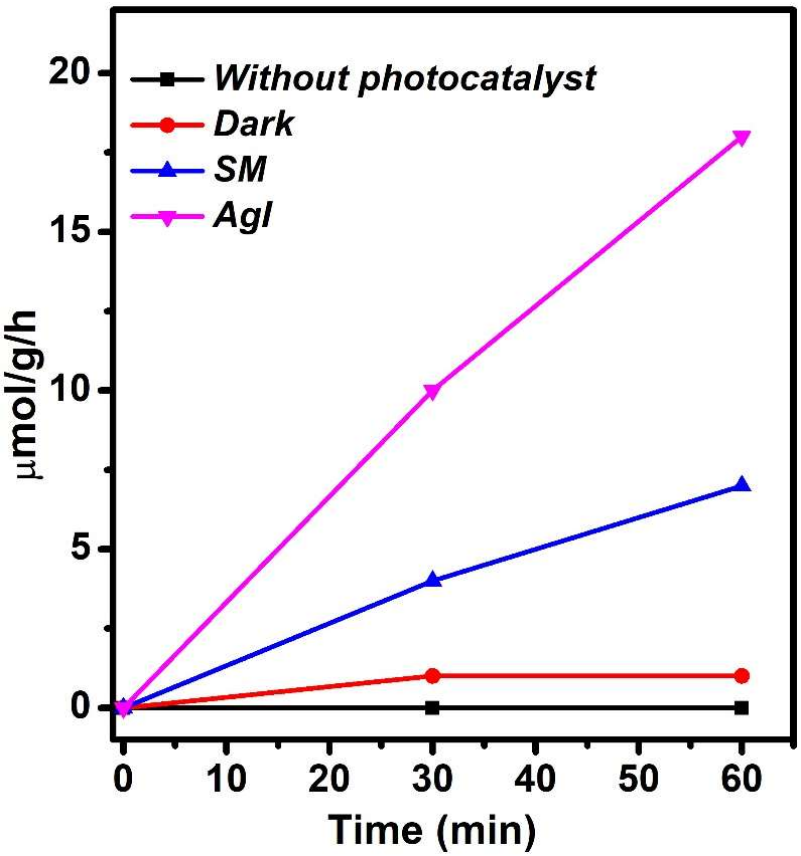

Figure 7.7. Photocatalytic H_2O_2 production under different conditions on pure SM and AgI photocatalysts.

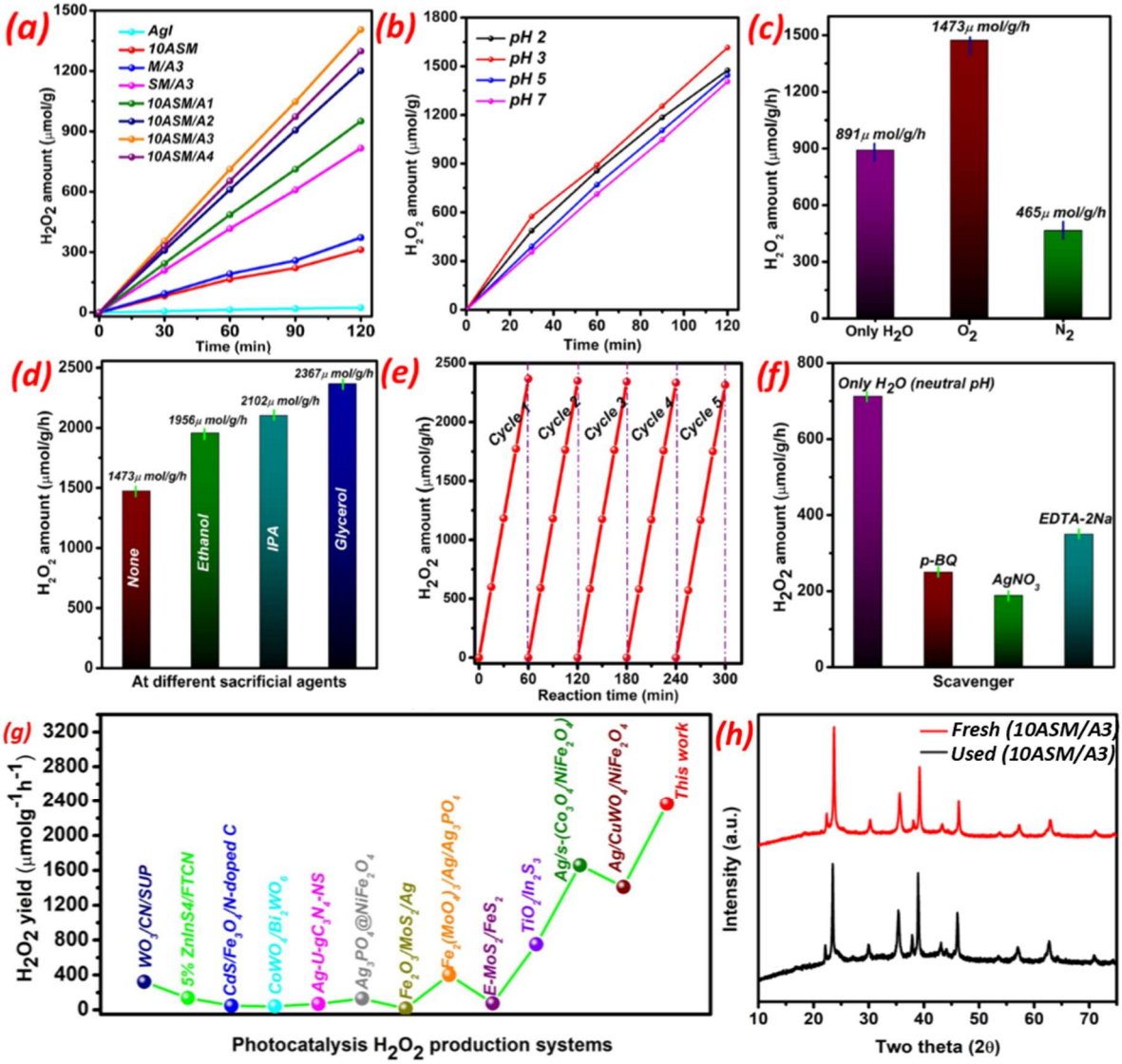

Figure 7.8. Photocatalytic H_2O_2 production **(a)** on different photocatalysts **(b)** at different pH on 10ASM/A3 photocatalysts **(c)** at different gas environments on 10ASM/A3 photocatalysts **(d)** at different sacrificial agents on 10ASM/A3 photocatalysts. **(e)** Recyclability on 10ASM/A3 **(f)** Scavenger experiment. **(g)** Comparison of photocatalytic H_2O_2 production with other recently published composite photocatalysts. **(h)** XRD pattern of fresh and used photocatalyst of 10ASM/A3.

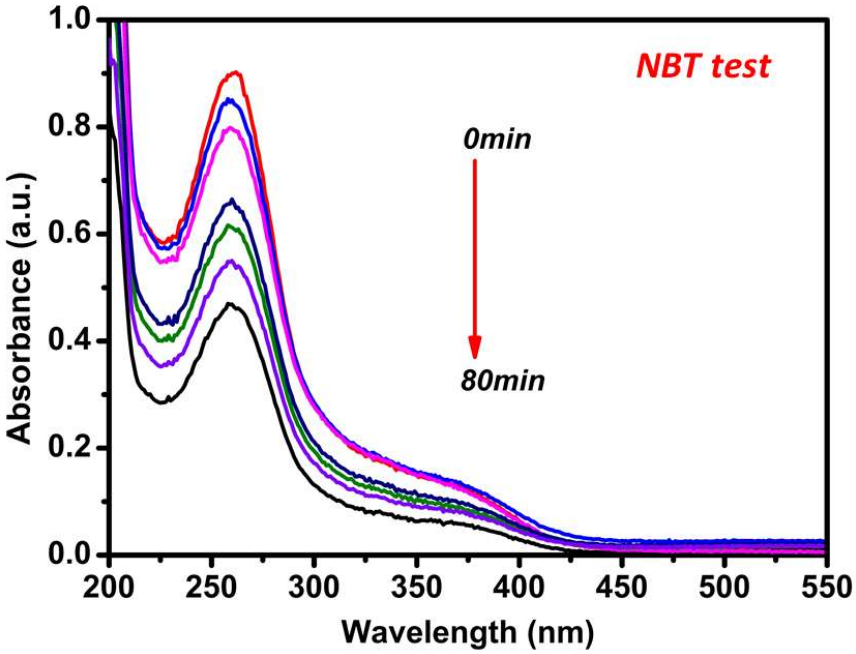

Figure 7.9. NBT test on 10ASM/A3 photocatalyst.

Table 7.2: Comparison of photocatalytic H_2O_2 production among different heterostructure composite photocatalysts**.**

Photocatalysts	Reaction condition	Light source	H_2O_2 yield ($\mu molg^{-1}h^{-1}$)	References
WO_3/CN-SUP	5% EtOH; O_2 purging	AM 1.5G	322	[132]
5% $ZnIn_2S_4$/FTCN50	10% EtOH	Visible light ($\lambda > 420$ nm)	135.98	[166]
CdS/Fe_3O_4/N-doped C	Only water	300W Xe lamp ($\lambda > 420$ nm)	47.28	[134]
$CoWO_4$@Bi_2WO_6	Only water; O_2 bubbling	300W Xe lamp ($\lambda > 420$ nm)	40	[249]

Ag@U-g-C_3N_4-NS	Only water	300W Xe lamp ($\lambda > 420$ nm)	67.50	[169]
Ag_3PO_4@$NiFe_2O_4$	75 vol% MeOH	300W Xe lamp ($\lambda > 420$ nm)	130	[64]
Fe_2O_3/MoS_2@Ag	Only water	Visible	15	[139]
$Fe_2(MoO_4)_3$/Ag/Ag_3PO_4	Methanol	UV/Visible light	400.8	[65]
E-MoS_2/FeS_2	Only water	300W Xe lamp	75	[98]
TiO_2 /In_2S_3	10% EtOH	300W Xe lamp (28 mW/cm^2)	752	[171]
10ASM/A3	5% Glycerol	Cool white LED	2367	This work

7.3.2. Photocatalytic in-situ H_2O_2 production for dark Fenton reaction

In section 7.2.4, we discussed the details of these experiments. The in-situ dark Fenton degradation performance of the as-prepared photocatalysts was conducted for TC degradation (Fig. 7.10a) under neutral pH conditions. Following a 120-minute photocatalytic reaction for H_2O_2 production, TC solution was promptly added into the quartz reaction reactor and placed in the dark. TC is hardly degraded in pure AgI and SM systems due to the negligible H_2O_2 yield. In contrast, the 10ASM/A3 photocatalyst demonstrated the highest degradation efficiency, achieving approximately 69% degradation of TC within 140 minutes, owing to its maximal H_2O_2 production yield compared to other prepared photocatalyst in this research. Figures 7.10 (b, c) illustrate the kinetics of TC degradation across various photocatalysts. In Figure 7.10b, the relationship between $\ln(C_0/C_t)$ and irradiation time (t) is depicted. The calculated values of k are presented in

Figure 7.10c. The excellent fitting indicates that the photocatalytic reaction follows first-order reaction kinetics. As shown in Figure 7.10c, the degradation rate constant of the 10ASM/A3 photocatalyst is approximately 12.5 and 6.5 times higher than those of pure SM and 10ASM photocatalysts, respectively.

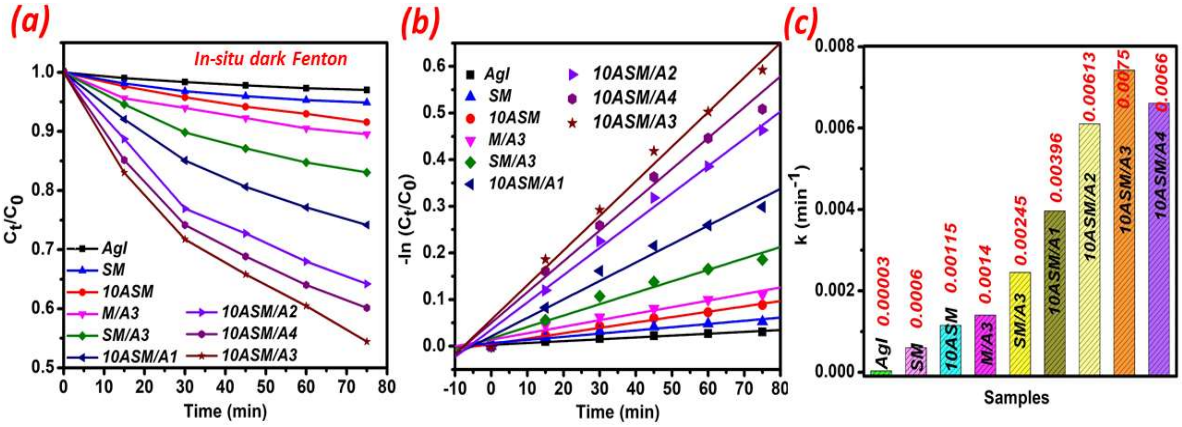

Figure. 7.10 (a, b) Comparison plot of in-situ dark Fenton TC degradation efficiencies with time on as-prepared photocatalysts and their corresponding first-order kinetics fitting **(c)** first-order rate constant.

7.3.3. In-situ H_2O_2 production for photo-Fenton reaction

Figure 7.11a illustrates the graphs depicting the degradation of tetracycline through in-situ photo-Fenton reaction under neutral pH conditions across different samples prepared in this investigation. The experimental procedures are outlined in the corresponding section 7.2.5. The degradation of TC occurred through the in situ generation of H_2O_2, and we have already quantified the amount of H_2O_2 produced over the various samples. While photocatalytic H_2O_2 production takes place, the decomposition of H_2O_2 occurs simultaneously through photogenerated electrons/Fe^{2+}, resulting in the generation of ·OH, which then engages in insitu Fenton-like degradation reactions. The in situ photo-Fenton degradation of TC on 10ASM/A3 displayed notably superior performance compared to both pristine samples and nanocomposites, primarily due to its significantly

higher generation of H_2O_2 over this specific photocatalyst (10ASM/A3). Figure 7.11b depicts the first-order rate kinetics observed in the photocatalytic insitu photo-Fenton degradation of tetracycline. As depicted in Fig. 7.11c, the kinetic constants ($k(min^{-1})$) of 10ASM/A3 were approximately 12 times greater than those of pure SM and 8.5 times higher than those of 10ASM photocatalysts. The in-situ Fenton degradation efficiency of tetracycline using 10ASM/A3 surpasses that of most previously reported heterostructure composite photocatalysts (see Table 7.3).

The recyclability of the photocatalyst (10ASM/A3) was assessed for in-situ photo-Fenton reactions. Fig. 7.11d illustrates the trend of tetracycline degradation over five consecutive cycles. Even after undergoing five cycles, the photocatalyst exhibited over 94% degradation of tetracycline, demonstrating its stability across repeated use. Following each cycle, the sample underwent washing, magnetic separation, drying, and subsequent utilization for the next cycle.

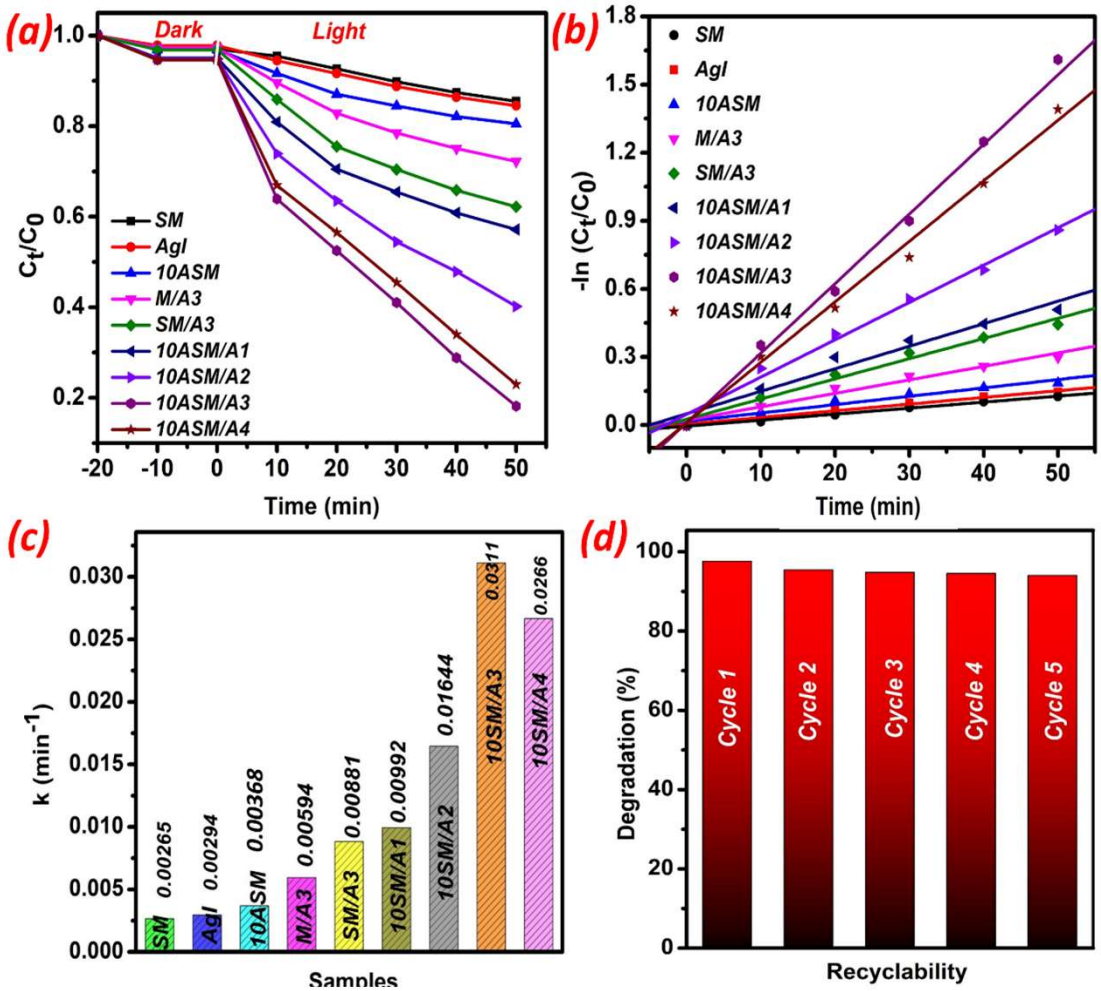

Figure 7.11. (a, b) Comparison plot of in-situ photo-Fenton TC degradation efficiencies with time on as-prepared photocatalysts and their corresponding kinetics plot**. (c)** First order rate constant **(d)** Recyclability test on 10ASM/A3 photocatalyst.

Table 7.3: Comparison of tetracycline degradation efficiency of in-situ H_2O_2 production and its utilization for photo-Fenton reaction among different photocatalysts

Photocatalysts	Reaction condition	Light source	Degradation % and time	Ref
FeOOH/UPCN	50 mg catalyst in 100 ml of 20 ppm oxytetracycline solution, pH-7	300W Xe lamp (λ > 420 nm)	86.23% (120 min)	[60]

NCQDs/MIL101 (Fe)	50 mg catalyst in 100 ml of 10 ppm TC solution; pH-natural	500W Xe lamp (λ > 420 nm)	100% (180min)	[173]
Fe_2O_3@C@1T/2H-MoS2	10 mg catalyst in 50 ml of 10 ppm TC solution, pH 6.5	300 W xenon lamp (λ > 420 nm)	91.4% (100 min)	[250]
Ag/s-(Co_3O_4/$NiFe_2O_4$)	0.24 mg catalyst in 5 ml of 10 ppm TC solution; pH-3	Cool white LED	~99% (400 min)	[49]
Ag/$CuWO_4$/$NiFe_2O_4$	0.24 mg catalyst in 5 ml of 10 ppm TC solution; pH-3	Cool white LED	93%(60min)	[48]
10ASM/AgI	5mg catalyst in 20 ml of 10 ppm TC solution	Cool white LED	96% (70min)	This work

7.3.4. Mechanism for photocatalytic H_2O_2 production

Compared to SM, AgI, 10ASM, and other composite photocatalysts, 10ASM/AgI, the composite containing 20wt% AgI with ASM demonstrates superior photocatalytic activity for both H_2O_2 production and in-situ Fenton reactions, including dark Fenton and photo-Fenton reactions. To elucidate the significantly improved H_2O_2 production observed over 10ASM/A3, the charge separation capabilities of the samples were significantly enhanced, as evidenced by 10ASM/A3 displaying lower photoluminescence intensity and the smallest semicircle in the EIS Nyquist plot compared to other prepared samples.

Photocatalytic production of H_2O_2 in pure water under neutral pH conditions without O_2 purging and sacrificial agents confirm that H_2O_2 is indeed generated from water oxidation. Control experiments revealed that even when N_2 was purged into the reaction mixture, a substantial amount of H_2O_2 was still generated (465 $\mu molg^{-1}h^{-1}$). Furthermore, scavenger tests demonstrated that $\bullet O_2^-$, h^+, and e^- are active species in the production of

H_2O_2. Here, the formation of H_2O_2 can be achieved through a two-step process of single-electron reduction of O_2, as illustrated in equations (7.2) and (7.3).

Water oxidation primarily occurs due to the starch functionalization of the Fe_3O_4 component, rendering the surface hydrophilic and promoting efficient water molecule adsorption. To evaluate the influence of starch functionalization on composite samples (10ASM/A3), we prepared an additional sample, denoted as M/A3 (Fe_3O_4 with 20 wt% AgI composite), without starch functionalization. Surprisingly, both H_2O_2 production and in-situ Fenton degradation of tetracycline were 4.5 times lower in the M/A3 composite compared to the 10ASM/A3 photocatalysts. These findings imply that starch functionalization results in an overall hydrophilic surface, facilitating water molecule adsorption and enhancing water oxidation efficiency. Consequently, H_2O_2 production is boosted, thereby improving the in-situ Fenton reaction within the 10ASM with AgI composite system.

To further investigate the water adsorption properties on M/A3 and 10ASM/A3 photocatalysts, water contact angle measurement is performed (Figure 7.12). After 2 seconds of contact with water droplets, the average contact angle of M/A3 was 58.9°, while that of 10ASM/A3 was 19.5°. As expected, the 10ASM/A3 photocatalyst reduced contact angle compared to M/A3. The starch functionalization led to enhanced hydrophilicity and dispersibility of photocatalysts in water. The sufficient water-photocatalyst contact suggests a high surface reaction probability.

The energy band positions and the semiconductor type of both SM and AgI have been determined based on the Tauc plot and the Mott-Schottky measurements. As illustrated in Figure 7.13, based on the Z-scheme heterojunction, when the 10ASM/A3 photocatalysts undergo illumination with visible light. This prompts the migration of

photogenerated electrons from the CB of starch-functionalized Fe_3O_4 to the metallic Ag NPs. Subsequently, these electrons electrostatically recombine with photogenerated holes (h^+) on the VB of the corresponding AgI component. Within the Z-scheme heterojunction framework, Ag NPs serve as a metallic bridge situated at the interface between SM and AgI and promote the rapid electron transfer from the CB of SM to VB of AgI. Under these conditions, the photogenerated electrons residing on the CB of AgI can engage in a reaction with adsorbed O_2, resulting in the formation of $\bullet O_2^-$ radicals. This occurrence arises from the more negative CB potential of AgI (-0.59 V vs. NHE) compared to the standard redox potential of $O_2/\bullet O_2^-$ (-0.33 V vs. NHE). Concurrently, the holes present on the VB of SM can activate H_2O, leading to the generation of proton (H^+) and O_2 molecules through water oxidation. This activation is facilitated by the VB potential of SM (+2.56 V vs. NHE), which is more positive than the H_2O/O_2 potential. Concurrently, the electron-rich CB reduces oxygen, resulting in the production of $\bullet O_2^-$, which then captures protons from the reaction medium, leading to the formation of H_2O_2 (Fig 7.13a).

To understand the function of metallic Ag NPs within the interface between SM and AgI for the photocatalytic production of H_2O_2, we prepared another photocatalyst, SM/A3 (without Ag loading), and investigated its performance in photocatalytic H_2O_2 production and in situ Fenton reaction. SM/A3 demonstrates lower photocatalytic activity compared to the Ag-loaded SM with AgI composites, potentially attributed to inadequate visible light absorption and slow charge transfer between SM and AgI.

$$\boldsymbol{O_2 + e^- \rightarrow \cdot O_2^-} \qquad \textit{(7.2)}$$

$$\boldsymbol{\cdot O_2^- + 2H^+ + e^- \rightarrow H_2O_2} \qquad \textit{(7.3)}$$

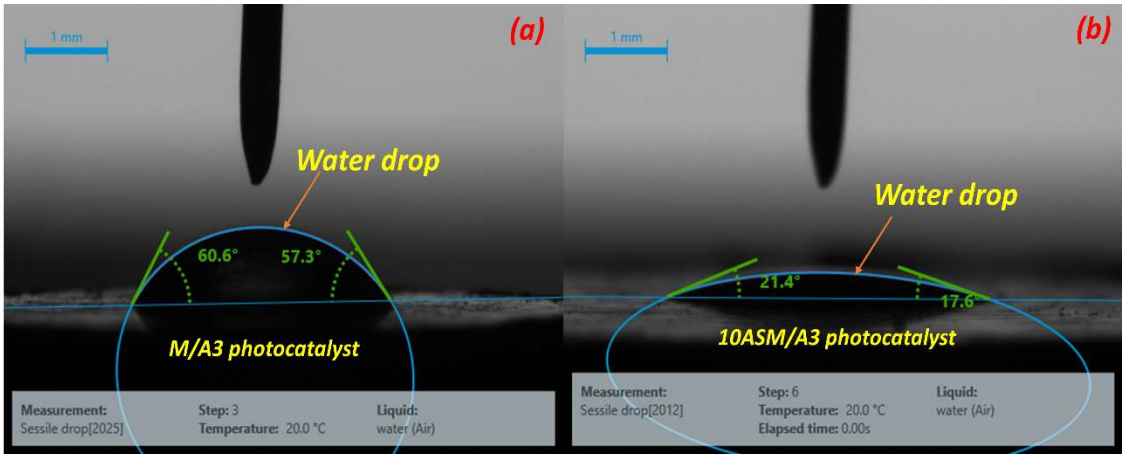

Figure 7.12. water contact angle measurement on **(a)** M/A3 and **(b)**10ASM/A3 photocatalysts

7.3.5. Mechanism of insitu Fenton reaction

To further investigate the potential of utilizing the generated •OH radicals, the in-situ dark Fenton and photo-Fenton degradation of TC were studied, as discussed earlier. Mechanism of in situ dark Fenton TC degradation on 10ASM/A3 photocatalytic system was shown in Fig. 7.13b. In the 10ASM/A3 nanocomposite system, lattice Fe^{2+} has the ability to trigger the production of ·OH and more Fe^{3+} through activation of H_2O_2 (as depicted in Equations 7.4 and 7.5). Subsequently, H_2O_2 facilitates the reduction of Fe^{3+} back to Fe^{2+}, continuing the cycle. Finally, the in situ generated •OH radicals attack to the TC molecules and breakdown into the small fragments.

$$Fe^{2+} + H_2O_2 \rightarrow Fe^{3+} + {\bullet}OH + OH^- \qquad (7.4)$$

$$Fe^{3+} + H_2O_2 \rightarrow Fe^{2+} + HO_2{\bullet} + H^+ \qquad (7.5)$$

$$Fe^{3+} + e^- \rightarrow Fe^{2+} \qquad (7.6)$$

Similarly, based on the above findings, the degradation of TC through in-situ photo-Fenton reaction may occur in two stages. In the first stage, under visible light exposure, lattice Fe^{2+} within the 10ASM/A3 system reacts with in-situ generated H_2O_2 to form •OH radicals and

Fe^{3+}, while simultaneously, photo-generated electrons reduce Fe^{3+} to Fe^{2+}, facilitating the cyclic conversion of Fe^{3+}/Fe^{2+} (as shown in Eq. 7.6). In the second stage, $\bullet O_2^-$ can be directly generated through the photo-generated single-electron reduction of O_2 (as indicated in Eq. 7.2), as confirmed by scavenger tests. The main reactive oxygen species, •OH and $\bullet O_2^-$, generated in the 10ASM/A3 system, directly contribute to TC degradation (Fig. 7.13c). The combined action of the photo-Fenton reaction and photocatalysis significantly enhances TC degradation compared to the dark Fenton reaction.

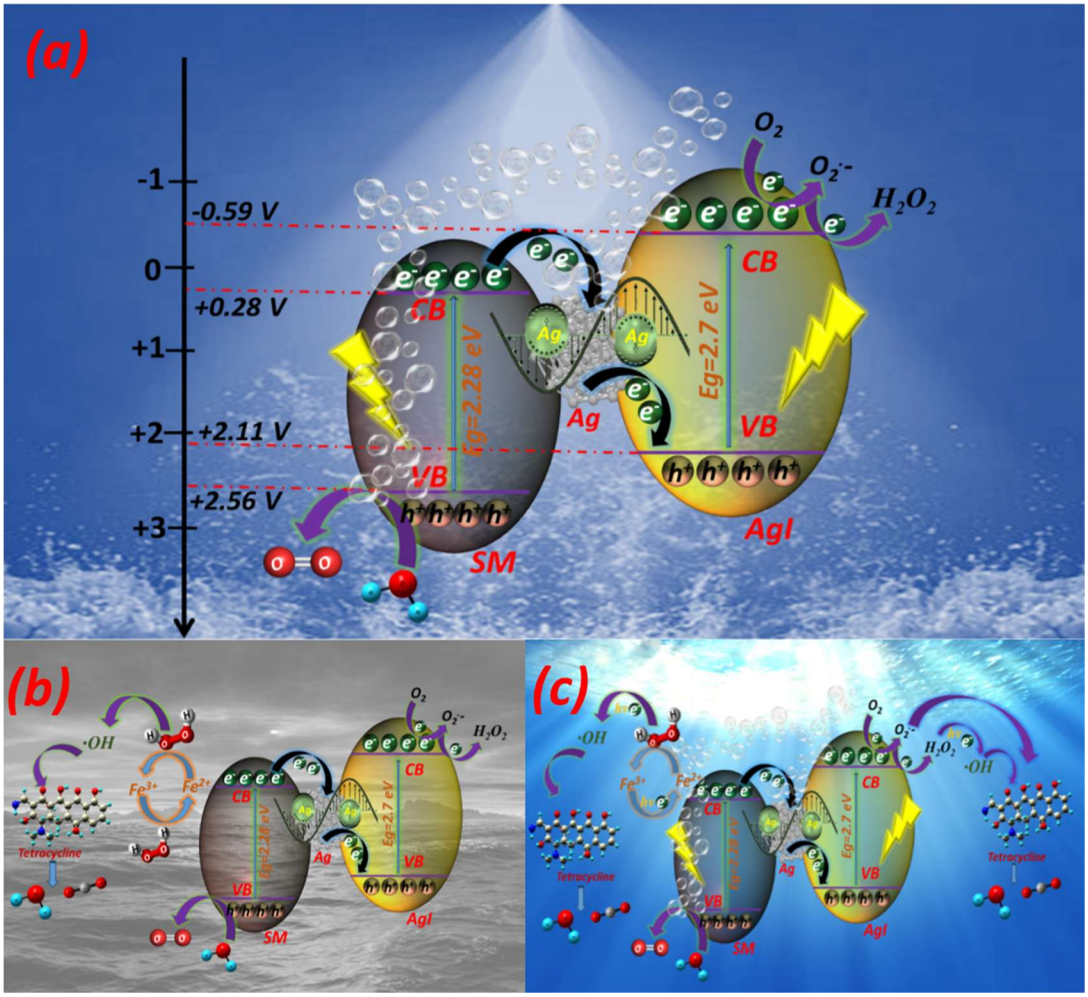

Figure 7.13. Proposed mechanism on 10ASM/A3 photocatalyst **(a)** photocatalytic H_2O_2 production**, (b)** in situ dark Fenton TC degradation, **(c)** in situ photo-Fenton TC degradation.

7.4 Conclusion

In summary, we successfully synthesized a 10ASM/AgI heterojunction composite photocatalyst via a facile stepwise precipitation method. In this heterostructure, AgI primarily serves as the reduction component, owing to its suitably positioned conduction band potential (–0.59 V vs. NHE). This enables photogenerated electrons from AgI to efficiently reduce O_2 to $\bullet O_2^-$ through a one-electron pathway, followed by proton-coupled electron transfer to generate H_2O_2 via an overall two-electron process. The strong reduction capability of AgI, combined with efficient charge separation at the heterojunction interface, significantly increases the availability of electrons for oxygen reduction. As a result, the engineered 10ASM/AgI composite exhibits excellent photocatalytic performance for H_2O_2 production in pure water, effectively utilizing integrated dual pathways that involve both the oxygen reduction reaction (ORR) and the water oxidation reaction (WOR).

Additionally, it exhibited high efficiency in situ dark Fenton and photo-Fenton reactions. Among the prepared samples, the composite containing 20 wt.% AgI (10ASM/A3) exhibited the highest H_2O_2 generation rate and the most effective in situ Fenton activity, attributed to its strong visible light absorption, efficient charge carrier separation and migration, and superior resistance to charge recombination. Additionally, water contact angle measurements revealed that starch functionalization on the 10ASM photocatalyst significantly enhanced its water adsorption affinity, which is crucial for promoting water oxidation. Control experiments using different sacrificial agents revealed that glycerol is an effective sacrificial agent for photocatalytic H_2O_2 production. Furthermore, free radical trapping experiments confirm that H_2O_2 generation on the 10ASM/AgI composite photocatalyst proceeds via a two-step single-electron ORR, with $\cdot O_2^-$ acting as key intermediate. Mechanistic studies reveal that the constructed heterojunction photocatalyst follows a Z-scheme pathway facilitated by the metallic Ag

interface between SM and AgI, which promotes effective energy coupling between the photogenerated electrons and the adsorption of O_2.